



Polycaprolactone-coated superparamagnetic iron oxide nanoparticles for *in vitro* magnetic hyperthermia therapy of cancer

Ziba Hedayatnasab^a, Ali Dabbagh^b, Faisal Abnisa^{c,*}, Wan Mohd Ashri Wan Daud^a

^a Department of Chemical Engineering, Faculty of Engineering, University of Malaya, Kuala Lumpur, Malaysia

^b School of Medicine, Faculty of Health and Medical Sciences, Taylor's University, Kuala Lumpur, Malaysia

^c Department of Chemical and Materials Engineering, Faculty of Engineering, King Abdulaziz University, Jeddah, Saudi Arabia

ARTICLE INFO

Keywords:

Superparamagnetic iron oxide nanoparticles
Micellar conformation
Core-shell
Specific absorption rate
In vitro magnetic hyperthermia
Cytotoxicity

ABSTRACT

Magnetic hyperthermia therapy of cancer is a promising alternative for the current chemotherapy and radiation options, due to its targeting capability and lower systemic toxicity. However, agglomeration vulnerability of the nano-heating agents in aqueous solutions, low control over the heat generation and dissipation at the target region, and eschewed clearance by the renal and reticuloendothelial systems remain as the main challenges for clinical translation of this approach. Here we report superparamagnetic iron oxide nanoparticles (SPIONs) were synthesized by using a single precursor, stabilized with a controlled micellar conformation, and coated with a thin polycaprolactone biopolymer shell to achieve enhanced cytocompatibility and thermosensitivity under external alternating magnetic field (AMF) of varied intensities. The *in vitro* investigations indicated a negligible influence of the polymer-coated SPIONs on cell viability of human liver cancer cells (HepG2) at a maximum concentration of $100 \mu\text{g}\cdot\text{mL}^{-1}$. However, the cell viability was reduced significantly to $40.1 \pm 0.9\%$ within the secure hyperthermia temperature range achieved by the heating effect of polymer-coated SPIONs in presence of AMF, depicting the on/off cytotoxicity phenomenon of polymer-coated SPIONs under AMF exposure. Therefore, the developed nanostructure presents a step-change as potential targeted nano-heating agents for new therapeutic options.

1. Introduction

Superparamagnetic iron oxide nanoparticles (SPIONs) have exhibited a propitious opportunity in biomedical applications from magnetic resonance imaging to drug delivery and magnetic hyperthermia therapy (MHT), owing to their promising therapeutic and diagnostic capabilities [1,2]. In particular, MHT is performed through infusion of SPION nanofluids in the presence of an external alternating magnetic field (AMF) to alter the metabolism of the heat shock proteins at the targeted tumor area, resulting in cellular degradation and apoptosis [3,4].

Nanoparticle-mediated cancer treatments necessitate adequate stability in aqueous media at neutral pH and physiological salinity. However, bare SPIONs are highly tendentious to self-agglomeration due to their strong electrostatic interactions, high surface energy, and vulnerability to air and moisture oxidation [5]. One potential approach to provide higher colloidal stability is surfactant-based surface modification of nanoparticles [1,6,7]. However, addition of excessive amounts of surfactants to the nanoparticle dispersions may induce

agglomeration of fine particles through charge neutralization, bridging and formation of surfactant-particle surface or via a combination of these mechanisms. The bridging mechanism occurs by attachment and absorbance of the surfactant chains on the nanoparticles surface, whereas a highly efficient surfactant with appropriate adsorption gives rise to surface saturation [8]. Therefore, the precise adjustment of the surfactant quantity is essential to prevent bridging and destabilization of nanoparticles, leading to the controlled particle size and improved dispersion. As SPIONs often possess a negative surface charge, surfactants with high cationic surface charges such as cetyltrimethylammonium bromide (CTAB) are necessary for their stabilization. CTAB consisted of a cationic organoamine with a 19-carbon tail and hydrophile-lipophile balance value of 10, which presents a substantial capability to separate precipitates in water medium [9]. CTAB may experimentally produce smaller particle size, which in turn gives rise to increased surface area, facilitating conjugation of varied therapeutic adjuvants through surface functionalization strategies [10].

A rapid opsonization and subsequent segregation by the immune system is another challenge during *in vivo* application of SPIONs. These

* Corresponding author.

E-mail addresses: z_hedayatnasab@yahoo.com (Z. Hedayatnasab), fta@kau.edu.sa (F. Abnisa).

nanoparticles are easily recognized as foreign bodies by the reticuloendothelial system (RES), instantly coated by plasma proteins and blood components, and rapidly cleared before reaching the targeted region [11]. Interestingly, a number of aliphatic linear polyesters including polyethylene glycol (PEG) [12], polyglycolic acid (PLGA) [13], and polylactic acid (PLA) [13] are known to provide ‘stealth’ characteristics, making nanoparticles invisible to the immune system. In particular, PEG is the most widely applied polymer in surface coating of SPIONs, which not only endows excellent stealth characteristics to the SPIONs and minimize RES sensitivity, but also improves their steric stability, dispersity, and biodistribution [14]. However, non-biodegradability and degradation under stress remain as the main drawbacks of PEG coatings [15]. PEG may also discourage interaction with the receptors on the targeted cell membranes and cause hypersensitivity through generation of antibodies, which neutralize the nanoparticles efficacy upon repeated administration [16].

More recently, polycaprolactone (PCL) has received increasing interests as a novel carrier of varied therapeutics due to its biodegradability, structural stability, partial crystallinity, non-toxicity, and amphiphilic feature [17]. PCL is also of particular interest due to its stealth and protein repellent characteristics, rendering minimized opsonization and RES sequestration [18]. When PCL is applied as surface coating on SPIONs, its partial crystallinity may confer it with potential to enhance the magnetic behavior due to ordered arrangement of magnetic moment in a single crystal.

Here we report development of PCL-coated SPIONs (magnetite; Fe_3O_4) with structural stability, uniform particle size, improved dispersity, cytocompatibility, and controlled heating under hyperthermia condition. A novel approach was applied for precipitation of SPIONs from a single iron precursor in a highly-controlled oxidative environment. SPIONs were further functionalized with a double-layered cationic CTAB surfactant to enhance their stability and provide proper surface functionality for biopolymer conjugation through electrostatic interactions. Thereupon, the CTAB-coated SPIONs were applied as a core and coated with a thin layer of PCL biopolymer through “graft-to” approach to achieve enhanced cytocompatibility and physicochemical properties for *in vitro* MHT on human hepatoma (HepG2) cell lines. Meanwhile, it was assumed that the polymeric coating may render a thermosensitive performance at the hyperthermia temperature (T_H) range due to the desirable low-melting temperature of PCL, resulting in enhanced induction heating efficiency of SPIONs as the treatment temperature was maintained within the secure T_H [19].

The effects of varied AMF strengths on induction heating capability of these core-shell nano-heating agents were investigated to obtain appropriate T_H profile. The core-shell nano-heating agents were further studied to quantify the cytocompatibility and *in vitro* cytotoxicity against HepG2 cells under hyperthermia condition. To the best of our knowledge, ad-micellar stabilized PCL-coated SPIONs have not yet been reported as a magnetic nano-heating agent for *in vitro* hyperthermia application.

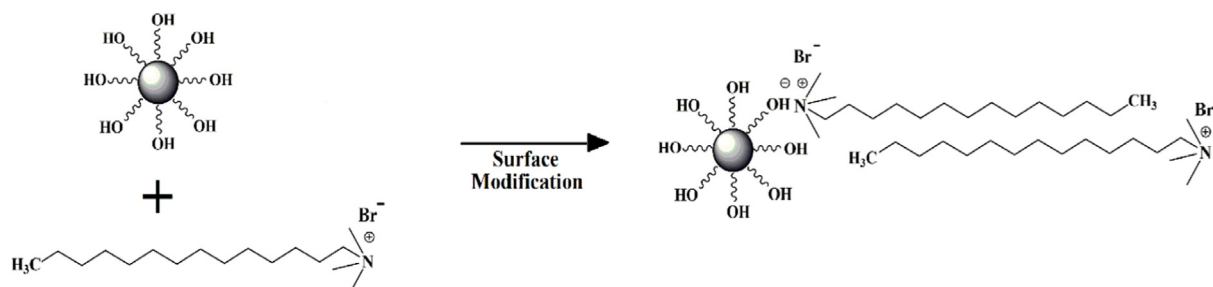


Fig. 1. A scheme of the chemical reaction for functionalization of iron oxide with CTAB cationic surfactant. An ad-micellar structure was synthesized to provide sufficient positive groups and further electrostatic attachment of PCL-d layer.

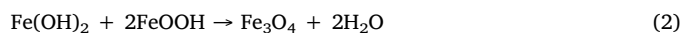
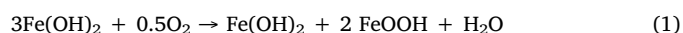
2. Materials and methods

2.1. Materials

The iron oxides were synthesized using ferrous chloride tetrahydrate ($\text{FeCl}_2 \cdot 4\text{H}_2\text{O}$ > 99%; R&M Chemicals) as the sole iron precursor, ammonium hydroxide solution ($\text{NH}_3 \cdot \text{H}_2\text{O}$ 28%; Sigma-Aldrich), as well as cetyltrimethylammonium bromide (CTAB; Sigma-Aldrich) as cationic surfactant. Polycaprolactone (PCL) with diol terminal groups (PCL-d, 2000 Da) and tetrahydrofuran (THF) solvent were purchased from Sigma-Aldrich. All the chemicals were in analytical grades and used without further modification or purification.

2.2. Synthesis procedure of iron oxide

Ferrous ions intrinsically show a great oxidation capability and rapidly undergo partial oxidation to ferric ions under partial oxidative environments according to the following reaction:



Therefore as a rule of thumb, iron oxides may be produced independent of using ferric precursor when 67% of the applied Fe^{2+} ions are oxidized to Fe^{3+} . This synthesis approach has adequate potential to produce iron oxides with lower costs and waste materials. Besides, reduced usages of chemical reagents incorporated in the synthesis reaction may lead to decreased synthesis complexity and enhanced physicochemical properties.

Iron oxides were synthesized by modification of the method reported in our previous work [5]. In order to synthesize iron oxides with the ferrous precursor, varied oxidative environments were preliminarily examined through alteration of the oxygen/nitrogen ($\text{O}_2:\text{N}_2$) flow ratios in the synthesis reactor (i.e. 0.3 to 0.6) and the $\text{O}_2:\text{N}_2$ ratio of 0.5 was chosen as the optimal oxidative environment for production of iron oxides with desirable physicochemical and magnetic properties. Briefly, in a typical experiment, 0.83 g of $\text{FeCl}_2 \cdot 4\text{H}_2\text{O}$ was dissolved in 2 mL of distilled water and volumed up by 50 mL of distilled water. Therein-after, $\text{NH}_3 \cdot \text{H}_2\text{O}$ was dropwise added to the mixture for further 30 min to obtain the black precipitates. At the end, the product was harvested with a strong magnet, washed with ethanol and distilled water to remove residual chloride ions and impurities, and finally dried in oven at 80 °C for 24 h.

2.3. CTAB functionalization of iron oxides

In order to enhance the iron oxides stability and provide functional groups for further polymer conjugation, an intermediate surface functionalization was carried out through the self-assembly of CTAB molecules on the particles surface. A schematic of the expected chemical interactions for production of CTAB-modified iron oxides is shown in Fig. 1. Based on the CTAB concentration in the medium, three main

micellar conformations such as hemi, ad, or mixed hemi-ad micelles could be obtained [20]. However due to the negative terminal groups of PCL-d, the ad-micellar structure was preferred in the current study to provide sufficient positive charge on the iron oxides surfaces for enhanced grafting of the biopolymer chains through electrostatic interactions. Therefore, five samples namely SPC₁, SPC₅, SPC₁₀, SPC₁₅, and SPC₂₀ with different CTAB amounts of 1, 5, 10, 15, 20 mg were used to determine the optimal surfactant quantity for provision of an ad-micellar structure on the particles surface. CTAB was added to the glass cylinder reactor containing iron oxides under vigorous stirring at 80 °C. The obtained product was dispersed and maintained in distilled water for further analyses.

2.4. Preparation of coated particles

Water-in-oil (W/O) emulsion was used for coating the particles with PCL-d biopolymer, where the oil phase comprised of THF solvent and PCL-d. Noticeably, coating the particles with amphiphilic or charged polymers gives rise to the reduction the oil-water interfacial tension and improve the stability of the emulsion in high-salinity environments, even at very low concentrations of nanoparticles [21]. In addition, the CTAB cationic surfactant acted as an emulsifier that formed the great stability of emulsions and created electrostatic interactions with the diol terminal groups of PCL-d, as shown in Fig. 2.

Briefly, 1 g of PCL-d was poured into 20 mL of THF and stirred for 30 min, meanwhile, 300 mg of modified-particles dissolved separately in 10 mL of distilled water using ultrasonication for 30 min. Thereafter, the oil and aqueous were mixed and vigorously stirred using a high-speed homogenizer at 10,000 rpm for 2 h to ensure that the PCL biopolymer was precipitated on the particles surface and produced the core-shell nanostructure. The obtained product was washed with THF, THF/distilled water (50:50), and thrice with distilled water until complete disappearance of impurities, followed by drying in oven at 80 °C for 24 h. A typical representation of the PCL-coated iron oxides preparation is illustrated in Fig. 3.

2.5. Characterization

The zeta potential (ζ) measurements (Zetasizer Nano ZEN, Malvern Instruments, Worcestershire, UK) were employed to measure the surface charge of the samples then determine the effect of surfactant concentration on the electrokinetic properties of the stabilized iron oxides with three times repeats for each sample. The high magnification surface morphologies were ascertained by transmission electron microscope (TEM; LEO Libra 120 kV, Carl Zeiss AG, Germany) as well as high-resolution transmission electron microscopy (HRTEM, field emission of 200 kV, Tecnai™ G2 20 S-TWIN FEI). Image analysis software (ImageJ) was used to obtain size distributions of particles from TEM images with information on mean size of each group that randomly-selected among at least 100 nanoparticles. The phase purity and crystal structure of the samples were also characterized using X-ray powder diffraction (XRD) patterns analysis (Philips PW1840, Amsterdam, the Netherlands) equipped with Cu-K α radiation ($\lambda = 1.542 \text{ \AA}$) with a graphite monochromator at the 2θ range from 10° to 80° . The chemical

functional groups of the magnetic samples were monitored using a Fourier transform infrared spectroscopy spectrometer (FTIR; Nicolet 6700, ThermoScientific, Madison, WI) through advanced direct surface contact technique in the range from 500 to 4000 cm^{-1} . The X-ray photoelectron spectroscopy (XPS) analysis was performed with a fully automated microprobe (PHI Quantera II, Ulvac-PHI, INC.) using Al-K α radiation with $\lambda = 1486.6 \text{ eV}$ operated at 25.6 W (beam diameter of $100 \mu\text{m}$). Low-resolution analysis was carried out through passing an energy of 280 eV with 1 eV per step to detect the chemical state of the elemental composition while high-resolution analysis performed over the binding energy range of 112 eV with 0.1 eV per step. The magnetic samples were prepared on a carbon tape supported by a stub holder. The charge correction was conducted at C 1s (carbon peak; C–C (1s)) before the deconvolution through the setting binding energy of C–C to 284.8 eV using MultiPak Spectrum software. The onset and peak phase transition temperatures were calculated through differential Scanning Calorimetry (DSC; Q1000 Perkin Elmer TA Instrument) at a heating rate of $20^\circ\text{C}/\text{min}$ using nitrogen air flow of 50 mL/min. In addition, thermogravimetric analysis (TGA; Q500 Perkin Elmer Instrument) of the dried samples were also performed by a NETZSCH STA 409 PC/PG (Selb, Germany) at a heating rate of 20°C from 20°C to 1000°C using a nitrogen air flow 50 mL/min to monitor the weight percentage of the polymer-coated particles. Magnetic characteristics of the powder samples were measured using a vibrating-sample magnetometer (VSM; model 7400 series, Lakeshore, Chicago, IL) in the magnetic field range of -8000 G to $+8000 \text{ G}$ (0.8 T) at ambient temperature.

2.6. Cell viability assay

The human liver carcinoma cells (HepG2 cell line) were resuscitated according to the standardized method in Dulbecco's Modified Eagle Medium (DMEM; Sigma Aldrich, USA) high glucose containing 4500 mg/L D-glucose, L-glutamine, 110 $\text{mg}\cdot\text{L}^{-1}$ sodium pyruvate, supplemented with 10% v/v fetal bovine serum (FBS; Sigma Aldrich, USA), 1% v/v penicillin/streptomycin (Gibco by Life Technologies) at 37°C in a 5% CO_2 humidified incubator and monitored daily. The growth media were changed in every three days and the cells were subcultured at 80% confluence through trypsinizing and were re-suspended in culture medium in a new flask or seeded in 96-well plates; hereupon, they were never encountered with the crowded conditions [22].

Cell viability and proliferation were observed by a dye-reduction assay known as the MTT (3-[4,5-dimethylthiazol-2-yl]-2,5-diphenyltetrazolium bromide) assay for the biomaterial toxicity detection. Briefly, the cells with a density of 1×10^5 cultured in a 96-well plate for 24 h for adhering to the plate surface then the cells were rinsed with phosphate-buffered saline (PBS; pH 7.4) in order to remove the disjoined cells and replace by fresh media. After that, the cells were treated with varied concentrations of iron oxide samples (100, 50, 25, 12.5, 6.25, 3.125, $1.5 \mu\text{g}\cdot\text{mL}^{-1}$) and were added into the wells, followed by adding PBS to each group (triplicate wells) and incubated at 37°C in a 5% CO_2 atmosphere for 24 and 48 h [23]. Control plates (the media with only cells) were also remained to monitor the potential changes in the culture media. The media were thereafter removed, and the cells were

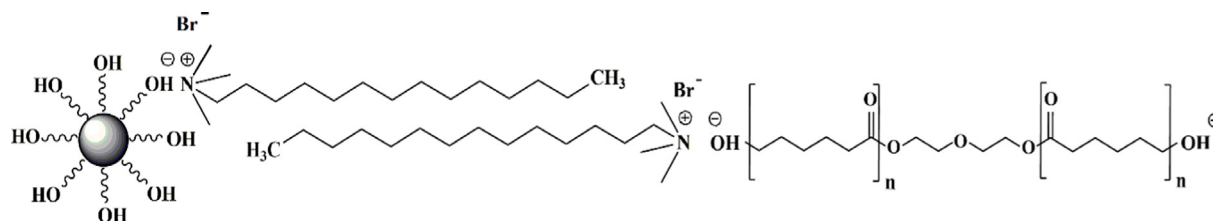


Fig. 2. A scheme of the attachment mechanism of PCL-d on CTAB-modified iron oxides. The presence of diol groups in the biopolymer formulation facilitated their attachment to the surfactant molecules via electrostatic interaction.

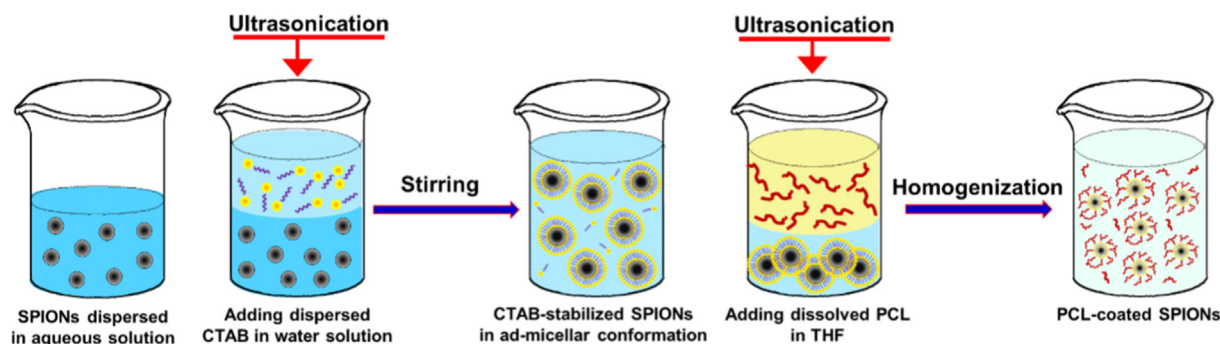


Fig. 3. A schematic view of the functionalization and coating of CTAB-modified iron oxides. An ad-micellar structure was formed on the particles surface and then CTAB molecules were attached with PCL-d chains.

washed with PBS to remove supernatant particles, followed by adding 10 μL of MTT dye solution to each well including control wells followed by 4 h incubation for metabolization of MTT with the samples and cell media. Meanwhile, the non-contamination of the cells was checked through an inverted microscope observation. The media were then removed through flicking the plates; thereby, only the anchored cells stayed in the wells. The water-insoluble formazan product extracted in 100 μL pure dimethyl sulfoxide (DMSO) was added to each well and incubated 2 h in the dark, followed by adding 25 μL Sorensen's glycine buffer as MTT stopper reactions and finally the absorbance was read with an iMark™ Microplate Absorbance Reader (Bio-Rad laboratories, Inc. USA) at 570 nm and reference filter at 630 nm. The cell viability was calculated using the following equation [23]:

$$\text{Cell Viability} = \frac{I_s}{I_c} \times 100\% \quad (3)$$

where I_s and I_c indicate the optical values of the cells which incubated with samples and control group, respectively.

2.7. Magnetic induction heating

The magnetic heating capability of iron oxides was assessed using an induction heating instrument (Easy Heat 8310, Ambrell, UK) with four varied electric currents of 50, 100, 150, and 200 A which were respectively corresponded to frequencies of 326, 318, 313, and 312 kHz. The particles dispersed in distilled water in conformity with the human body structure with a solution concentration of 1 $\text{mg}\cdot\text{mL}^{-1}$ [24] was positioned in the center of a short helical coil with 8 turns having inner diameter of 2.54 cm and 6 cm long connected to external AMF [4], which was equipped to water circulation cable to maintain the temperature of the coil at ambient temperature. The magnetic field strength, (H) were determined from the following equation [25,26]:

$$H = \frac{n \cdot i}{L} \left(\frac{A}{m} \right) \quad (4)$$

where n , i , and L are defined as the number of turns, applied current (A) and the diameter of the turn (m) for the helical coil, respectively. The calculated values of the magnetic field strength at 50, 100, 150 and 200 A were 15.74, 31.49, 47.24, and 62.99 $\text{kA}\cdot\text{m}^{-1}$, respectively. The samples were exposed to external AMF and the time-temperature profiles obtained over 5400 s.

The heating efficiency was quantitatively estimated through the specific absorption rate (SAR) measurement which attributed to the amount of received energy converted into the heat and calculated through following equation [28]:

$$\text{SAR} = \left(\frac{\sum_i C_i m_i}{m_{\text{Fe}}} \right) \left(\frac{dT}{dt} \right) \quad (5)$$

where C_i is the specific heat capacity of the colloidal dispersion (which is the combination of medium with values of 4.18 $\text{J}\cdot\text{g}^{-1}\cdot\text{K}^{-1}$, and

SPIONs sample (iron oxides and PCL biopolymer with values 0.65 $\text{J}\cdot\text{g}^{-1}\cdot\text{K}^{-1}$, and 0.08 $\text{J}\cdot\text{g}^{-1}\cdot\text{K}^{-1}$, respectively)), and m_i defines as the total mass of the colloidal dispersion which comprises of medium, SPIONs sample (iron oxides, and PCL biopolymer) with the concentration of 1 $\text{mg}\cdot\text{mL}^{-1}$. Consequently, $(\sum_i C_i m_i) = (C_{\text{medium}} \times m_{\text{medium}}) + (C_{\text{sample}} \times m_{\text{sample}})$. In addition, m_{Fe} indicates the iron mass per unit mass of SPIONs sample [29]. The molecular weight of PCL-diol is $M_w \sim 2000$ and molar mass of Fe_3O_4 is 231.533 $\text{g}\cdot\text{mol}^{-1}$, and dT/dt represents the initial slope of the temperature profile.

2.8. In vitro magnetic hyperthermia on the HepG2 cells

The *in vitro* heating capability of the samples in cell growth inhibit was quantitatively evaluated through MTT assay. The HepG2 cells with the density of 1×10^5 cells/mL were seeded in a 96-well plate and incubated until cell attachment. After 24 h, the cultured HepG2 cells were divided into control group and treated group with SPIONs samples at 100 $\mu\text{g}\cdot\text{mL}^{-1}$ and then incubated for 4 h [30]. The *in vitro* magnetic hyperthermia tests were performed on both groups under the exposure of the external AMF at 31.49 and 47.24 $\text{kA}\cdot\text{m}^{-1}$, based on the obtained results from induction heating section. After the exposure, the cells were incubated for 24 h, thenceforward, the cells were placed in a 96-well plate, followed by MTT assay to compare the cell viabilities of the treated cells exposed to different AMF strengths with those of control groups.

2.9. Data analysis

At least three experimental replications were performed for all experiments and the obtained results were expressed as the means \pm standard deviation (SD). Statistical analysis was carried out using one-way ANOVA and post hoc Tukey corrections through Statistical Package for Social Sciences software (SPSS; version 25, SPSS Inc., Chicago, IL, USA). Results were considered significant at 95% confidence interval ($P < 0.05$).

3. Results and discussion

3.1. Characterization of surfactant micellar conformation

Based on the concentrations, surfactant molecules often arrange in three main micellar configurations on the nanoparticles surface including hemi, ad, and mixed hemi-ad micelles (Fig. 4). In the hemi micellar arrangement, a surfactant monolayer is formed on the nanoparticles surface via coulombic attraction. With the increment of the absorbed surfactant, the hydrophobic interactions among the hydrocarbon chains of the surfactant molecules lead to their bilayer arrangement on the nanoparticles surface and formation of the ad-micellar configuration. A mixed hemi-ad micelle array is also formed at

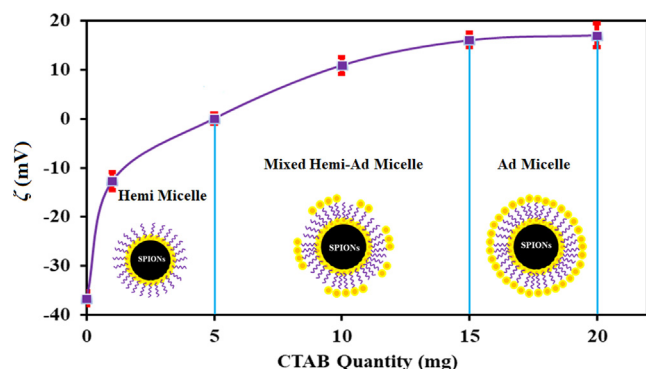


Fig. 4. Different configurations of surfactant molecules around the iron oxide particles at varied CTAB quantities. Three main micellar structures are determined based on changes of the ζ -values of samples.

intermediate surfactant concentrations, with both coulombic and hydrophobic interactions [20,31]. The formation of each configuration could be determined via ζ measurements, where the low and high ζ -values indicate the presence of hemi and ad micelles, respectively.

Fig. 4 illustrates the ζ changes of iron oxide samples with addition of varied surfactant quantities. When CTAB was added into the synthesis solution, their positively-charged hydrophilic heads electrostatically bonded to the hydroxyl groups of iron oxide, resulting in neutral charges. Therefore, the ζ -value progressively raised from -30 ± 3 mV (for bare iron oxide at pH ~ 9) to zero at CTAB quantity of 5 mL, confirming formation of hemi micelles around particles through electrostatic interaction. Notably, the hydrophobic interactions among the tail groups of the surfactant molecules is the primary driving force for their ad-micellar configuration in the aqueous medium. Therefore with increase of the CTAB concentration, free hydrophobic polar tails assemble together via chain-to-chain reactions and the polar heads become exposed, leading to positive ζ -values [20,31]. This trend continued to reach the maximum ζ -value of $+16 \pm 2$ mV in CTAB concentration of 15 mg, indicating formation of ad-micellar configuration of the CTAB molecules on the particles surface. Thereby, this surfactant quantity (SPC₁₅) was considered as the critical concentration for ad-micellar configuration (CaMC) and the optimal amount for surface modification of iron oxides for further attachment of the PCL-d chains.

When PCL-d was added into the solution, the ζ -value significantly reduced to around -8 ± 2 mV ($P < 0.05$), implying PCL-d coating layer was formed around particles surface through electrostatic interactions. The presence of unreacted diol groups on the polymer changes probably contributed in generation of negative charges on the coated iron oxides.

3.2. Morphological studies

The morphological characteristics of bare iron oxides, SPC₁₅, and PCL-SPC₁₅ are illustrated in Fig. 5a-d. The TEM micrographs clearly showed all the synthesized nanoparticles with a uniformly distributed spherical shape. Meanwhile, surface modification by the cationic surfactant could slightly improve the particle dispersity in the aqueous medium, probably due to particle-particle interactions [6,29]. According to Fig. 5c, no significant alteration in nanoparticles dispersity and agglomeration was observed by further coating of the SPC₁₅ particles with PCL biopolymer. A typical TEM image from an individual nanoparticle with higher magnification is also illustrated in Fig. 5d, which obviously confirms formation of a core-shell structure comprised of iron oxide core and PCL shell. Fig. 6a-b depicts the particle size distribution of bare iron oxides, SPC₁₅, and PCL-SPC₁₅ matched well with Gauss fitting curve. As a result of polymer coating, the mean diameter of nanoparticles was increased from 18 ± 2 to 21 ± 3 nm,

indicating formation of a 3 nm polymer coating on the bare iron oxide nanoparticles.

3.3. Phase structure

The obtained XRD patterns on bare iron oxide, SPC₁₅, and PCL-SPC₁₅ are illustrated in Fig. 7a-c. The XRD patterns confirmed formation of a single magnetite phase (JCPDS 00-001-1111) with cubic spinel and Fd3-m space group in all samples, implying the negligible effects of CTAB and PCL on the crystalline phase of iron oxides. The XRD diffraction peaks of all samples observed at 2θ values of 18.45° , 30.37° , 35.74° , 43.41° , 53.93° , 57.40° , 62.98° , and 74.46° respectively corresponded to (1 1 1), (2 2 0), (3 1 1), (4 0 0), (4 2 2), (5 1 1), (4 4 0), and (5 3 3) family planes of magnetite (PDF 89-4319).

The XRD Patterns of PCL-SPC₁₅ illustrates the presence of two crystalline polymeric and metallic phases. The added peaks at 2θ of 21.4° and 23.7° (Fig. 7c) are represented the crystallographic planes of (1 1 1) and (2 2 0), respectively [32].

The HRTEM image in Fig. 8 also depicts an interlayer spacing of 0.254 nm for Fe₃O₄ cores in PCL-SPC₁₅, which is well-matched with the (3 1 1) planes of magnetite (PDF 89-4319) possessing an interlayer spacing of 0.251 nm.

3.4. Chemical investigation

The FTIR spectra of bare Fe₃O₄, pure CTAB, SPC₁₅, pure PCL biopolymer, and PCL-SPC₁₅ are shown in Fig. 9a-e. FT-IR spectra of bare Fe₃O₄ clearly displays absorption peaks of 3401.22 and 1627.56 cm^{-1} , which were respectively characteristics of stretching and bending vibrations of hydroxyl functional group (H—O—H), required for electrostatic assembly of CTAB molecules [33]. The peaks in the low-frequency region from 500 to 800 cm^{-1} , particularly at 583.83 cm^{-1} attributed to Fe—O absorption bands which confirmed the presence of the magnetite. The presence of 3017.13 cm^{-1} band could be attributed to the vibrations of the ammonium moiety in CTAB. Additionally, the peaks at around 2848.39 and 2916.37 cm^{-1} were related to symmetric and antisymmetric C—H vibration bands of the —CH₂ group which derived from the long aliphatic tail of CTAB. The peaks at 1461.31 and 959.90 cm^{-1} were associated with asymmetric stretching vibration of N⁺—CH₃, besides the peak 718.36 cm^{-1} might be corresponded to Br[−] [6].

FTIR spectrum of PCL biopolymer possessed a strong band at 1719.73 cm^{-1} that could be assigned to carbonyl stretching (C=O groups). In addition, the bands at 2941.44 and 2863.81 cm^{-1} were related to asymmetric and symmetric stretching vibration of aliphatic C—H groups, while absorption bands at 1238.09 and 1159.51 cm^{-1} were belonged to asymmetric and symmetric stretching of C—O—C group in PCL, respectively [34]. The recorded spectra for PCL-SPC₁₅ (Fig. 9e) was identical to that of pure PCL and exhibited the same characteristic vibration bands of Fe₃O₄ with slightly lower intensities owing to the presence of active components.

Fig. 10a depicts the low-resolution XPS survey spectra of PCL-SPC₁₅ while high-resolution C 1s, O 1s, and Fe 2p XPS spectra of the PCL-SPC₁₅ are shown in Fig. 10b-d. The Fe 2p spectrum (Fig. 10d) comprised of the doublet Fe 2p_{1/2} and Fe 2p_{3/2} possessed the binding energy values of 723.72 eV and 710.44 eV respectively, which were considered as the common peaks for magnetite. The peaks from such spectra were probably deconvoluted into two components correlated with Fe³⁺ and Fe²⁺ ions. These results implied that the composition of the Fe₃O₄ core was unaffected by surfactant and polymer modifications. The O 1s spectrum (Fig. 10c) could be also deconvoluted into four peaks ascribed to the oxygen atoms from Fe—O, OH (Fe₂O₃), C—O/C=O, and COOH located at 529.82 , 530.29 , 531.46 and 532.38 eV, respectively [35]. The C 1s spectrum (Fig. 10b) included the contribution of four components peaks situated at 284.58 , 285.49 , 286.65 and 288.53 eV were respectively corresponded to carbon atoms of C—C, C—O, C=O

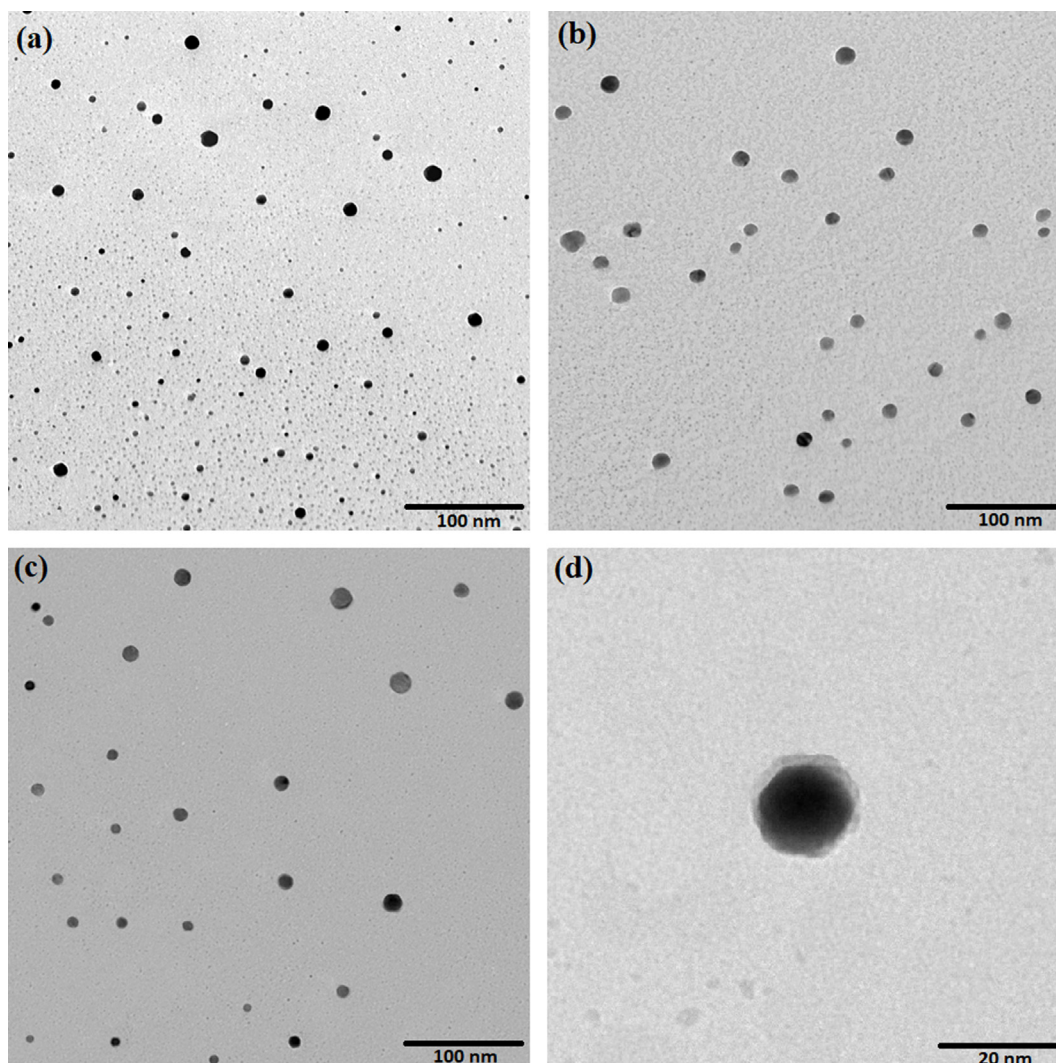


Fig. 5. The TEM images of a) bare iron oxide, b) SPC₁₅, and c, d) PCL-SPC₁₅ with different magnifications. The core-shell structure of PCL-SPC₁₅ is obviously observed.

and COOH from PCL, which were well-matched to previous other report [36]. Both XRD and XPS studies confirmed that PCL biopolymer was successfully coated on the SPC₁₅ surface.

3.5. Thermal analysis

DSC technique was performed to evaluate the phase transition behavior of pure PCL and PCL-SPC₁₅ samples. As shown in Fig. 11a, the peak temperature of endothermic phase transition for pure PCL was

observed at $52.1 \pm 2^\circ\text{C}$ [37]. However, the onset temperature of this phase transition was initiated at $45.4 \pm 2^\circ\text{C}$, implying that the melting point of PCL polymer with molecular weight of 2000 Da was within the upper hyperthermia range (45 to 52°C). The DSC thermograms of the PCL-SPC₁₅ also elucidated insignificant alterations of the onset and peak temperatures of endothermic phase transition of PCL after coating on the metallic core. This range of phase transition temperature in the PCL-SPC₁₅ particles confirmed their appropriacy for cancer therapy under hyperthermia condition.

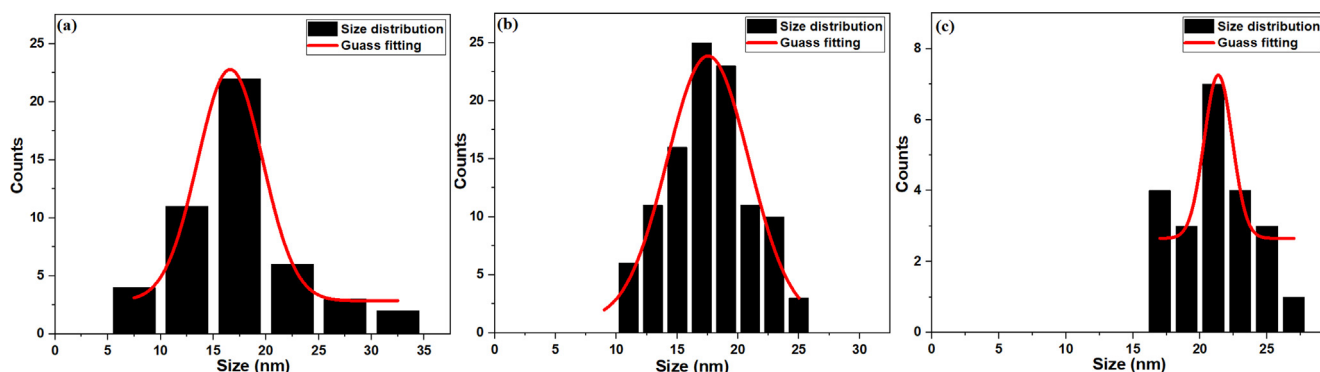


Fig. 6. The size distribution of a) bare iron oxide, b) SPC₁₅, and c) PCL-SPC₁₅.

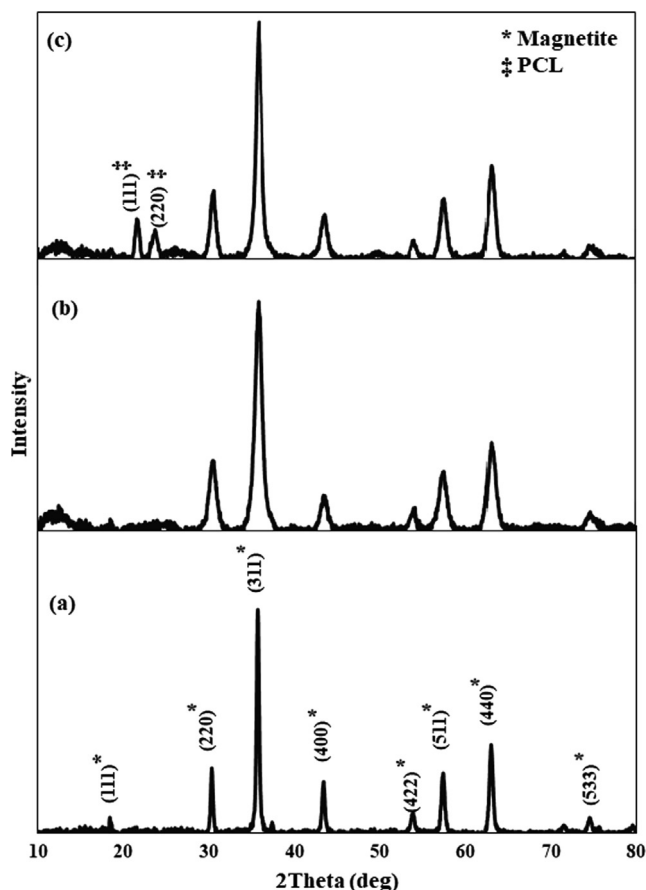


Fig. 7. The XRD patterns of a) bare iron oxide, b) SPC₁₅, and c) PCL-SPC₁₅. The peaks at 21.4° and 23.7°, which represent the crystallographic planes of PCL, indicated the formation of biopolymer coating on the nanoparticles surface.

TGA analysis was also carried out to determine the quantities of CTAB and PCL in the core-shell nanostructure. As shown in Fig. 11b, the curve of SPC₁₅ depicts a small weight loss of around 3%, which could be attributed to the evaporation of CTAB. On the contrary, the TGA measurement of PCL-SPC₁₅ exhibited a mass loss of approximately 12% in two phases. The first phase of weight loss correlated with CTAB evaporation at temperatures below 300 °C, while an additional weight

loss of approximately 9% at 300–400 °C in the second phase attributed to degradation of PCL to CO₂, CO, and H₂O [38]. The obtained PCL quantity was comparable with the value obtainable from the TEM images (9%), based on the theoretical densities of Fe₃O₄ and PCL.

3.6. Magnetic studies

The obtained magnetic properties of bare Fe₃O₄, SPC₁₅, and PCL-SPC₁₅ are provided in Table 1. The symmetry and reversibility of the hysteresis curves are depicted in Fig. 12 which are indicative their superparamagnetic behavior with extremely low coercivity (H_c), nearly zero remanence (M_r) and relative remanence (M_r/M_s). These findings were consistent with the TEM results, which indicated the potential superparamagnetic behavior of these particles due to their average particle sizes of below 20–30 nm and single-domain large magnetic moments [39].

Further, two distinct features were perceived from the magnetic properties. Firstly, the saturation magnetization (M_s) value descended after both stabilization and polymer coating, probably due to the nonmagnetic natures of both CTAB and PCL. Due to a low amount of surfactant, no significant reduction in the M_s -value from 72 ± 3 emu·g⁻¹ to 69 ± 5 emu·g⁻¹ was observed after surface modification of SPIONs ($P > 0.05$). The M_s value was further decreased to 64 ± 4 emu·g⁻¹ when PCL was coated on the SPC₁₅ cores. However, this alteration was also statistically negligible, possibly due to the semi-crystalline structure of PCL biopolymer, which may lead to more oriented magnetic moments. Noteworthy that M_s -values of above 50 emu·g⁻¹ are considered pivotal for nano-heating agents in MHT application in order to provide sufficient induction heating powers required for destruction of malignancies [40].

Secondly, the H_c -value of bare SPIONs was almost twice of SPC₁₅ and PCL-SPC₁₅ because of relatively higher particle agglomeration and friction relaxation loss. Besides, the interparticle interactions could also elucidate this effect through high surface-area-to-volume of bare SPIONs that increase the exchange interactions between individual particles and consequently enhanced surface energy, effective magnetic volume, and coercivity [41]. Meanwhile, surface modification could weaken the interparticle interactions by increasing the distance between the individual particles, giving rise to the coercivity reduction.

3.7. Cytotoxicity study

The cell metabolic activity of PCL-SPC₁₅ at a series of varied concentrations up to 100 µg·mL⁻¹ were assessed against HepG2 carcinoma

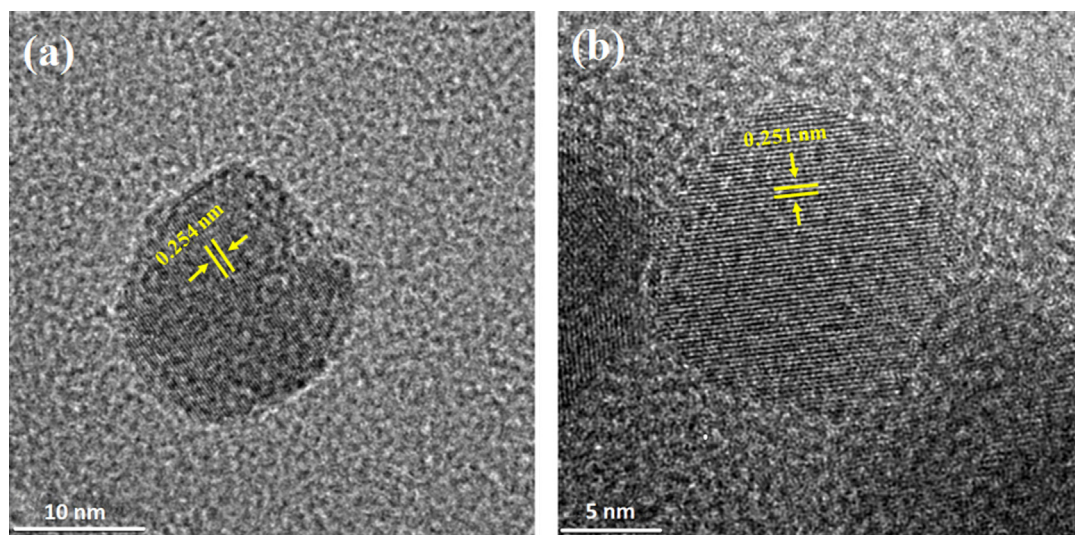


Fig. 8. HRTEM images of a) bare iron oxide and b) PCL-SPC₁₅. The interlayer spacings in both bare and coated Fe₃O₄ closely matched with that of magnetite.

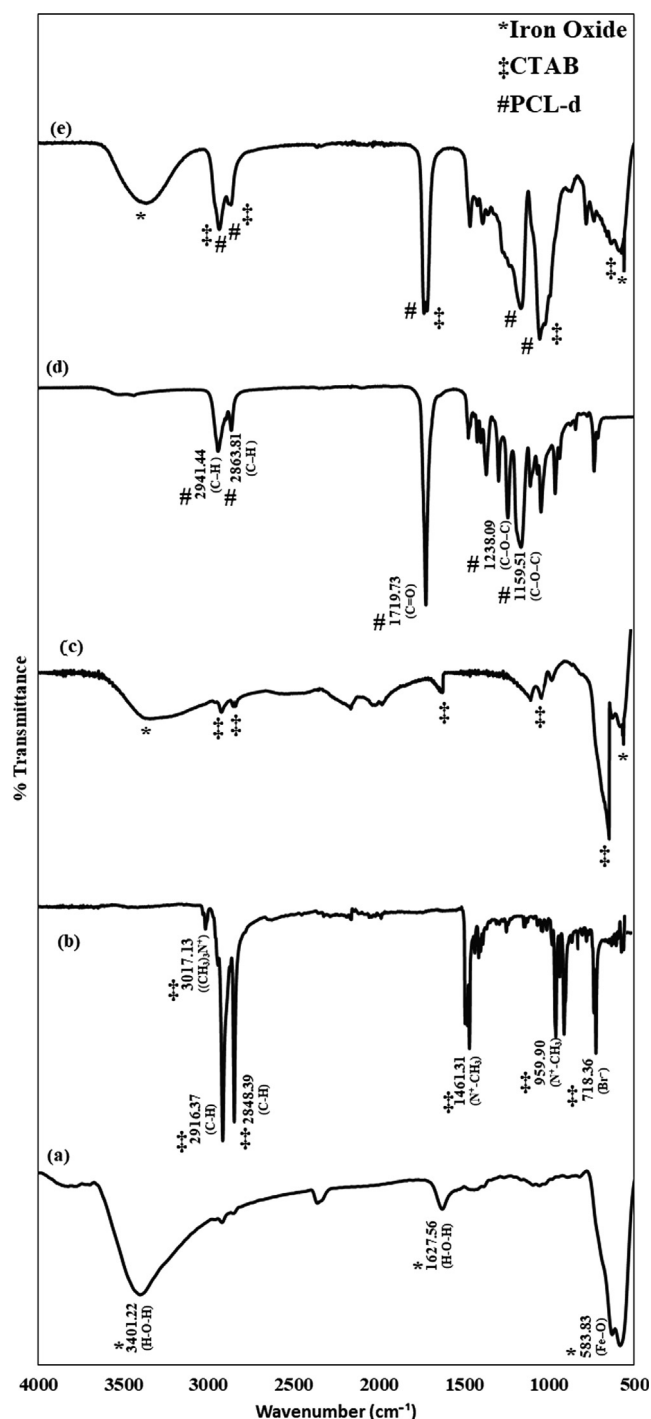


Fig. 9. FTIR spectra of a) bare iron oxide, b) pure CTAB, c) SPC₁₅, d) PCL-d, and e) PCL-SPC₁₅. The spectrum of PCL-SPC₁₅ matched the spectra of PCL and SPC₁₅. The *, ‡, and # symbols represent the specific bonds of iron oxide, CTAB, and PCL-d respectively, indicated the formation of their functional groups on the PCL-SPC₁₅ surface.

cells through an MTT assay. The observation of morphological changes in cells indicated that PCL-SPC₁₅ concentrations of up to 100 $\mu\text{g}\cdot\text{mL}^{-1}$ dispossessed antiproliferative activity against HepG2 cells in incubation intervals of 24 and 48 h. Therefore, PCL-SPC₁₅ induced no significant cytotoxicity towards HepG2 cells with possessing a cell viability above $95 \pm 0.01\%$ at the highest concentration (shown in Fig. 13). Moreover, this value was significantly greater as compared to that of bare SPIONs ($90.37 \pm 0.03\%$) observed in preliminary studies with a similar concentration, conforming the positive influence of PCL coating

on the cytocompatibility of SPIONs. This finding was also in consonance a previous study which reported an enhanced cytocompatibility when chitosan cores were coated by PCL biopolymer shells [42].

3.8. Magnetic hyperthermia studies

In an attempt to correlate the magnetic and structural properties of PCL-SPC₁₅ with the hyperthermia performance, the heating capability of these nanoparticles was examined through measuring the temperature rise upon applying external AMF with different strengths. The temperature profiles of the aqueous solutions containing 1 $\text{mg}\cdot\text{mL}^{-1}$ of PCL-SPC₁₅ exposed to varied AMF strengths are presented in Fig. 14. Analogous heating behaviors at varied magnetic strengths were observed, where a temperature stability was illuminated at the initial 80 sec (stage I), followed by abrupt temperature rise till heating intervals of approximately 200 sec (stage II). The medium temperature continued to increase till approximately 1500 sec (stage III) and then, no significant temperature rise was observed in the aqueous medium (stage IV). The most influential effect of field strength was in the stage II, where the slopes of temperature rise (dT/dt) at this stage was almost doubled with increase of the AMF strength from $15.47 \text{ kA}\cdot\text{m}^{-1}$ to $62.99 \text{ kA}\cdot\text{m}^{-1}$. Therefore, the dT/dt values at stage II were determined for measurement of SAR values at each magnetic strength. Accordingly, the calculated SAR values were respectively 99.17 ± 1.1 , 152.65 ± 1.2 , 201.21 ± 0.7 , and $255.12 \pm 0.8 \text{ W}\cdot\text{g}^{-1}$ for AMF strengths of 15.74, 31.49, 47.24, and $62.99 \text{ kA}\cdot\text{m}^{-1}$.

The hyperthermia treatments are recommended to be carried out in time intervals of below 900 s to minimize potential disorders on the human body. This is due to the inner temperature of SPIONs is approximately twice that of the aqueous medium, hence longer residence of stealth SPIONs may enhance protein absorption on the SPIONs surfaces, leading to higher agglomeration and reduced colloidal stability [43]. Moreover, longer time exposure to AMF may incur irreversible damage to the surrounding tissues [44]. Therefore, treatment repetition in shorter time intervals is not only avoid the side effects but even boost the hyperthermia efficiency by completing tumor regression [45]. The obtained temperatures after exposure to AMF strengths of 15.74, 31.49, 47.2, and $62.99 \text{ kA}\cdot\text{m}^{-1}$ over 900 s were $39.5 \pm 0.8^\circ\text{C}$, $44.5 \pm 0.5^\circ\text{C}$, $48.1 \pm 0.9^\circ\text{C}$, and $53.5 \pm 0.6^\circ\text{C}$, respectively. Therefore, the strength value of $31.49 \text{ kA}\cdot\text{m}^{-1}$ and a heating interval of 900 sec were determined as the minimum AMF parameters for generation of sufficient heat within the secure T_H range (the band area in Fig. 14). This strength could also initiate phase transition of the PCL shell (Fig. 11) and sustain the medium temperature within T_H range throughout the treatment time. Although the applied magnetic strength of $31.49 \text{ kA}\cdot\text{m}^{-1}$ and frequency 318 kHz exceeded the recommended threshold value $H \times f < 5 \times 10^9 \text{ A}\cdot\text{m}^{-1}\cdot\text{s}^{-1}$ for the secure clinical purposes [46], lower magnetic strength e.g. $15.74 \text{ kA}\cdot\text{m}^{-1}$ might require a higher concentration of ferrofluid to produce adequate heat in killing cancer cells within the secure T_H [47]. In addition, higher concentrations may give rise to smaller SAR values due to the possibility of nanoparticles aggregation. Therefore, minimized concentration of magnetic nano-heating agent with remarkable SAR value are necessitated to perform successful hyperthermia treatment and also prevent the eddy currents that cause unpredictable disorders in patients during the clinical trials. It is also noteworthy that the synthesized PCL-SPC₁₅ presented a superior SAR value ($255.12 \text{ W}\cdot\text{g}^{-1}$) in comparison with other reported SPION coatings including, poly-L-lysine [48], carboxydextran [49], PCL mat [38], chitosan [26] and PEG [24], which might be due to its greater capability in provision of well-dispersed SPIONs. Besides, the thermo-responsive nature of PCL biopolymer in the T_H range was considered as an extra benefit in the heating power enhancement.

SPIONs in single-domain state induce both Néel and Brownian relaxations under the AMF exposure [50] to heat up the entire perimeter surrounding through the flipping motion of the magnetic moment

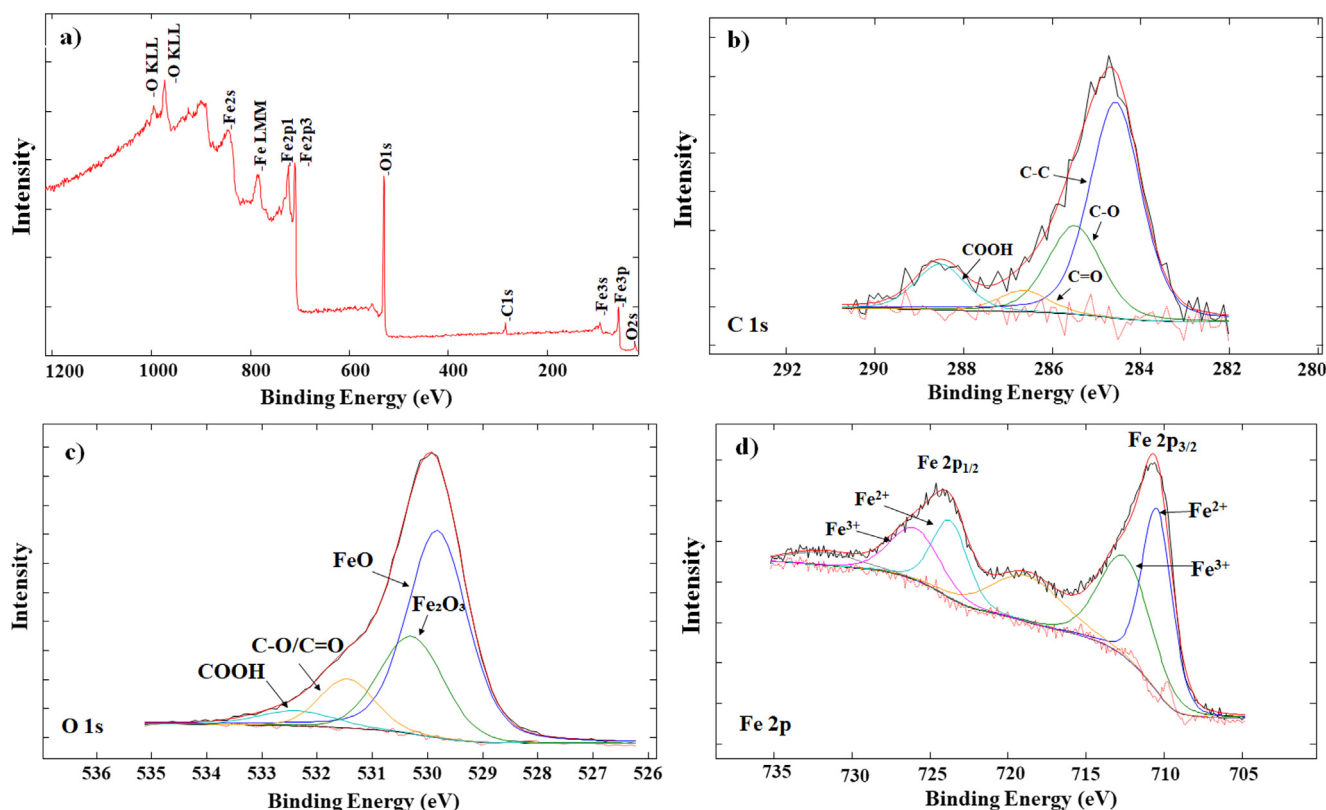


Fig. 10. The XPS spectra of PCL-SPC₁₅. a) Low-resolution survey spectrum, b) High-resolution C 1s XPS spectrum c) High-resolution O 1s XPS spectrum, and d) High-resolution Fe 2p XPS spectrum. Fe 2p_{1/2} and Fe 2p_{3/2} peaks are related to the magnetite phase and the carbon peaks in C 1s spectrum are assigned to the presence of PCL coating on the nanoparticles surface.

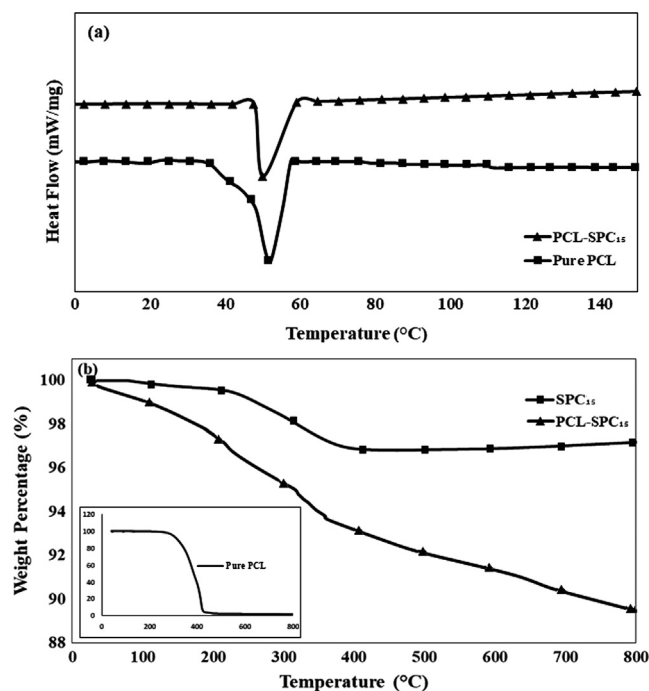


Fig. 11. (a) DSC thermograms of pure PCL and PCL-SPC₁₅. The thermal phase transition of polymer unaffected by attachment to the surface of PCL-SPC₁₅. (b) TGA curves of pure PCL, SPC₁₅ and PCL-SPC₁₅. Two phases of weight loss in PCL-SPC₁₅ curve indicate the presence of CTAB and also PCL coating on the nanoparticles surface.

Table 1
Magnetic properties of bare SPIONs, SPC₁₅, and PCL-SPC₁₅.

Samples	M_s (emu·g ⁻¹)	M_r (emu·g ⁻¹)	H_c (G)	M_r/M_s
Bare SPIONs	72 ± 3	2 ± 0.2	10 ± 0.3	0.0248
SPC ₁₅	69 ± 5	1 ± 0.1	5 ± 0.2	0.0278
PCL-SPC ₁₅	64 ± 4	1 ± 0.2	5 ± 0.2	0.0135

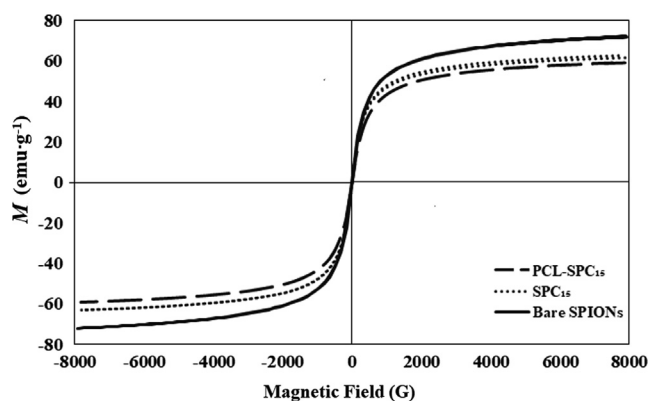


Fig. 12. The hysteresis curves of bare SPIONs, SPC₁₅, and PCL-SPC₁₅ nanoparticles. Although surface modifications reduced M_s and H_c , rendered such sample as a promising nano-heating agent for MHT.

within the crystal and the random motion of nanoparticles suspended in a solution, respectively. In general, when the nanoparticles diameter is below a critical range of 20–30 nm, the Néel relaxation time ' τ_N ' becomes predominant, whereas the Brownian relaxation time ' τ_B ' is considered as primarily heating mechanism for larger diameters. For

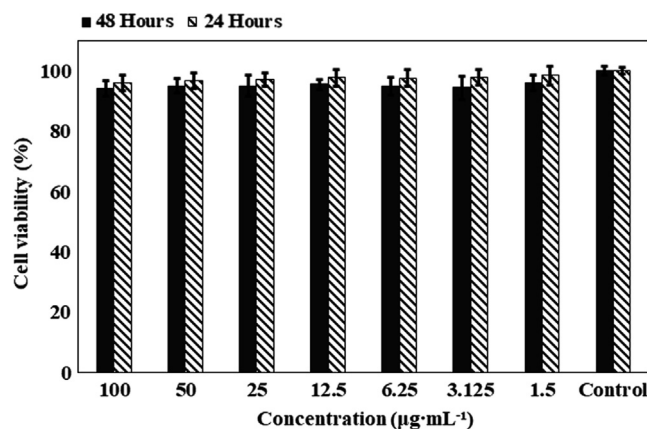


Fig. 13. Cell viability profiles of HepG2 cells treated with different concentrations of PCL-SPC₁₅ for 24 and 48 h. The concentrations variation and incubation interval showed no significant effects on the cell viability ($P > 0.05$) at 95% confidence level [94.88–99.79%].

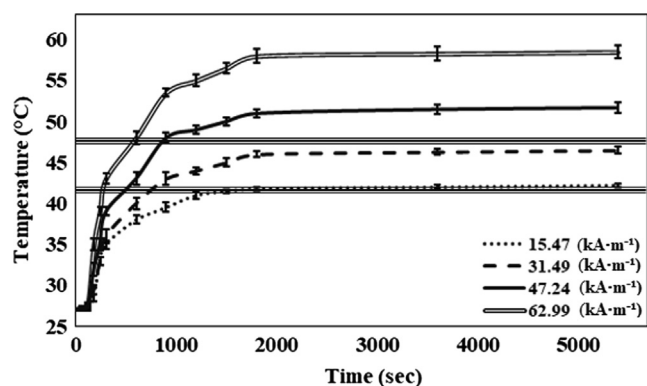


Fig. 14. The thermal profile of PCL-SPC₁₅ samples at varied AMF strengths. Increasing the concentration affected the saturation temperature upward. The AMF strength of 31.49 kA/m could only induce heating power within the secure hyperthermia range.

particle diameters in the range of 20–30 nm, the effective relaxation time is defined as $\tau_{\text{eff}} = (\tau_N \tau_B) / (\tau_N + \tau_B)$ [51]. As a result, the core diameters of bare SPIONs and PCL-SPC₁₅ synthesized in this study designated that the produced heat was due to Néel relaxation. Moreover, the produced heat through the viscous friction between the rotating nanoparticles and their surrounding might be raised for larger particle diameter, implying a negligible effect of the Brownian mechanism. The anisotropy constant and particle aggregation also contribute in the heating mechanism. Deatsch and Evans [52] demonstrated that the dominant heating loss assigned to the one with faster relaxation time. PCL-SPC₁₅ with mean particle diameter of around 20 nm was therefore indicated a shorter relaxation time of $\sim 10^{-7}$ s, meaning that τ_N might be occurred faster as compared to τ_B . However, τ_N is affected by the interparticle spacing as the energy barrier raised with enhancement of particle interactions. Therefore, the reduced dipolar interactions and increased interparticle spacings via incorporation of surfactant and coating layers may result in hampered Néel mechanism, which is typically considered as the dominant heating loss mechanism in MHT.

3.9. In vitro hyperthermia test on HepG2

Fig. 15 illustrates the comparison between the temperature profiles of the control group and the cell media containing 100 $\mu\text{g}\cdot\text{mL}^{-1}$ PCL-SPC₁₅ under the exposure of 31.49 and 47.24 $\text{kA}\cdot\text{m}^{-1}$ magnetic strengths over 900 sec, which respectively raised the medium temperature to 43.2 ± 0.3 °C and 46.1 ± 0.5 °C. The viability of HepG2

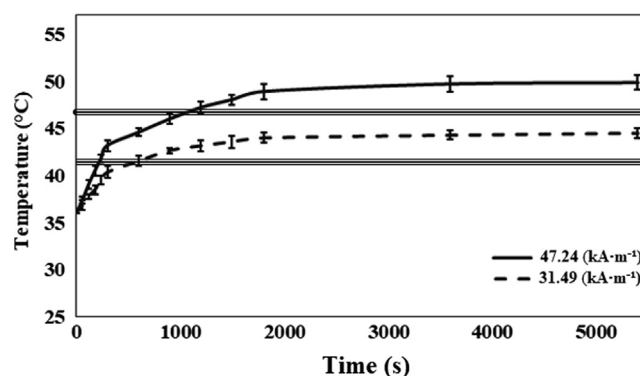


Fig. 15. The temperature profile of HepG2 carcinoma cells with and without PCL-SPC₁₅ during exposure to varied AMF strengths. The minimal magnetic field of 31–47 kA/m could only render PCL-SPC₁₅ with adequate heating capability to retain the desirable T_H (the band area).

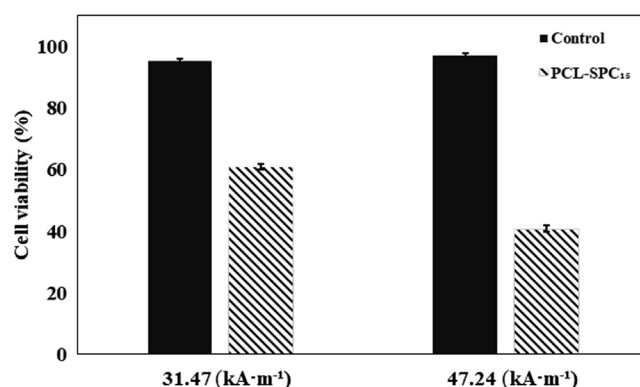


Fig. 16. Cytotoxicity profiles of HepG2 cells treated with PCL-SPC₁₅ exposed to varied AMF strengths, as quantified by MTT assay. The percentage cell viabilities of HepG2 were represented relative to the control cells.

cells was quantified instantaneously by MTT assay on the control group and PCL-SPC₁₅ samples to prevent external factors effects. The cell viability responses of HepG2 cells were investigated in incubation interval 24 h shown in Fig. 16. In spite of exposing to different AMF strengths, the control groups possessed the cell viabilities above 93% in comparison with the control group in the absence of AMF, indicating that the AMF applied in this research was in the safe range. Moreover, the cell viability results implied that neither SPIONs alone nor AMF alone with varied strengths could inhibit the cell growth, which were in a good agreement with other research study [30].

However, the cell viabilities were significantly lessened to $60.9 \pm 0.8\%$ and $40.1 \pm 0.9\%$ ($P < 0.05$) when the HepG2 cells were treated with PCL-SPC₁₅ and exposed to the AMF strengths of 31.49 $\text{kA}\cdot\text{m}^{-1}$ and 47.24 $\text{kA}\cdot\text{m}^{-1}$ in incubation interval of 24 h, respectively. Thereby, the principal mechanism for the cell growth inhibition was the produced heat by PCL-SPC₁₅ nanoparticles under AMF exposure. It assumed that the produced heat possesses adequate capability to increase the reactive oxygen species and thus denature cell division [23]. These significant reductions in cell viability of HepG2 treated with PCL-SPC₁₅ through induction heating process confirmed the hypothesis that this novel magnetic nano-heating agent comprised of SPIONs core and PCL biopolymer shell demonstrated a successful hyperthermia performance.

4. Conclusions

This work is the first report on development of ad-micellar stabilized magnetic nano-heating agents with PCL biopolymer coating for *in vitro* hyperthermia application. The significant hyperthermia efficiency

of PCL-SPC₁₅ was due to their intrinsic superparamagnetic property, stabilizing effect of CTAB ad micelles, combined with the thermo-responsive nature of PCL biopolymer. The data presented here demonstrated the significant heating capability of PCL-SPC₁₅, which incurred a potent cytotoxic effect on HepG2 carcinoma cells under AMF exposures with appropriate strengths.

The future direction of present research involves development of magnetic drug delivery systems with active targeting of the carcinoma cells. Moreover, the thermosensitive performance of PCL coating could endow the magnetically thermal-triggered drug-releasing ability under AMF exposure. In fact, the cytotoxic effect of this magnetic nano-heating agent would be enhanced through the synergistic effects of hyperthermia as well as chemotherapy that induced by PCL-coated SPIONs and drugs, respectively. This will involve the use of both magnetic nanoparticles and drugs which can indeed consider as a promising cancer-therapeutic alternative modality to address the crucial issues of current chemotherapy.

CRediT authorship contribution statement

Ziba Hedayatnasab: Conceptualization, Writing - original draft, Methodology, Investigation, Writing - review & editing, Validation, Data curation, Formal analysis. **Ali Dabbagh:** Methodology, Writing - review & editing, Data curation, Resources, Validation. **Faisal Abnisa:** Methodology, Writing - review & editing, Supervision, Visualization, Data curation, Project administration. **Wan Mohd Ashri Wan Daud:** Conceptualization, Supervision, Funding acquisition, Resources.

Declaration of Competing Interest

The authors declare that they have no known competing financial interests or personal relationships that could have appeared to influence the work reported in this paper.

Acknowledgement

This project was funded by the Deanship of Scientific Research (DSR), King Abdulaziz University, Jeddah, under grant No. (DF-437-829-1441). The authors, therefore, gratefully acknowledge DSR technical and financial support.

References

- [1] Z. Hedayatnasab, F. Abnisa, W.M.A. Wan Daud, Review on magnetic nanoparticles for magnetic nanofluid hyperthermia application, *Mater. Des.* 123 (2017) 174–196.
- [2] A. Amirshaghghi, L. Yan, J. Miller, Y. Daniel, J.M. Stein, T.M. Busch, Z. Cheng, A. Tsourkas, Chlorin e6-coated superparamagnetic iron oxide nanoparticle (SPION) nanoclusters as a theranostic agent for dual-mode imaging and photodynamic therapy, *Sci. Rep.* 9 (1) (2019) 2613.
- [3] S.L. Berry, K. Walker, C. Hoskins, N.D. Telling, H.P. Price, Nanoparticle-mediated magnetic hyperthermia is an effective method for killing the human-infective protozoan parasite *Leishmania mexicana* in vitro, *Sci. Rep.* 9 (1) (2019) 1059.
- [4] T.K. Nguyen, H.T.T. Duong, R. Selvanayagam, C. Boyer, N. Barraud, Iron oxide nanoparticle-mediated hyperthermia stimulates dispersal in bacterial biofilms and enhances antibiotic efficacy, *Sci. Rep.* 5 (1) (2015) 18385.
- [5] Z. Hedayatnasab, A. Dabbagh, F. Abnisa, N.H. Abu Ksaim, W.M.A. Wan Daud, Synthesis of highly stable superparamagnetic iron oxide nanoparticles under mild alkaline reagents and anaerobic condition, *Nanosci. Nanotechnol. Lett.* 11 (7) (2019) 985–990.
- [6] S.A. Elfeky, S.E. Mahmoud, A.F. Youssef, Applications of CTAB modified magnetic nanoparticles for removal of chromium (VI) from contaminated water, *J. Adv. Res.* 8 (4) (2017) 435–443.
- [7] C. Boyer, M.R. Whittaker, V. Bulmus, J. Liu, T.P. Davis, The design and utility of polymer-stabilized iron-oxide nanoparticles for nanomedicine applications, *NPG Asia Mater.* 2 (1) (2010) 23–30.
- [8] E. Günster, S. İçi, N. Öztekin, F.B. Erim, Ö.I. Ece, N. Güngör, Effect of cationic surfactant adsorption on the rheological and surface properties of bentonite dispersions, *J. Colloid Interface Sci.* 303 (1) (2006) 137–141.
- [9] E.E. Yalcinkaya, D. Puglia, E. Fortunati, F. Bertoglio, G. Bruni, L. Visai, J.M. Kenny, Cellulose nanocrystals as templates for cetyltrimethylammonium bromide mediated synthesis of Ag nanoparticles and their novel use in PLA films, *Carbohydr. Polym.* 157 (2017) 1557–1567.
- [10] L. Gan, Z. Lu, D. Cao, Z. Chen, Effects of cetyltrimethylammonium bromide on the morphology of green synthesized Fe₃O₄ nanoparticles used to remove phosphate, *Mater. Sci. Eng., C* 82 (2018) 41–45.
- [11] P. Aggarwal, J.B. Hall, C.B. McLeland, M.A. Dobrovolskaia, S.E. McNeil, Nanoparticle interaction with plasma proteins as it relates to particle biodistribution, biocompatibility and therapeutic efficacy, *Adv. Drug Deliv. Rev.* 61 (6) (2009) 428–437.
- [12] A.A. Sebak, Limitations of pegylated nanocarriers: unfavourable physicochemical properties, biodistribution patterns and cellular and subcellular fates, *Int. J. Appl. Pharm.* 10 (5) (2018) 6–12.
- [13] C.L. Ferreira, C.A. Valente, M.L. Zanini, B. Sgarioni, P.H. Ferreira Tondo, P.C. Chagastelles, J. Braga, M.M. Campos, J.A. Malmonge, N.R. de Souza Basso, Biocompatible PCL/PLGA/polypyrrole composites for regenerating nerves, *Macromol. Symp.* 383 (1) (2019) 1800028.
- [14] S. Khoei, G. Yousefzadeh, A. Kavand, Preparation of dual-targeted redox-responsive nanogels based on pegylated sorbitan for targeted and antitumor drug delivery, *Eur. Polym. J.* 95 (2017) 448–461.
- [15] K. Knop, R. Hoogenboom, D. Fischer, U.S. Schubert, Poly(ethylene glycol) in Drug Delivery: Pros and Cons as Well as Potential Alternatives, *Angew. Chem. Int. Ed.* 49 (36) (2010) 6288–6308.
- [16] S. Zhang, C. Tang, C. Yin, Effects of poly(ethylene glycol) grafting density on the tumor targeting efficacy of nanoparticles with ligand modification, *Drug Deliv.* 22 (2) (2015) 182–190.
- [17] M.P. Arrieta, L. Peponi, Polyurethane based on PLA and PCL incorporated with catechin: Structural, thermal and mechanical characterization, *Eur. Polym. J.* 89 (2017) 174–184.
- [18] S.M. Espinoza, H.I. Patil, E. San Martin Martinez, R. Casañas Pimentel, P.P. Ige, Poly-ε-caprolactone (PCL), a promising polymer for pharmaceutical and biomedical applications: Focus on nanomedicine in cancer, *Int. J. Polym. Mater.* 69 (2) (2020) 85–126.
- [19] K. Van Butsele, M. Morille, C. Passirani, P. Legras, J.-P. Benoit, S. Varshney, R. Jérôme, C. Jérôme, Stealth properties of poly(ethylene oxide)-based triblock copolymer micelles: a prerequisite for a pH-triggered targeting system, *Acta Biomater.* 7 (10) (2011) 3700–3707.
- [20] M. Amiri-Aref, J.B. Raoof, F. Kiekens, K. De Wael, Mixed hemi/ad-micelles coated magnetic nanoparticles for the entrapment of hemoglobin at the surface of a screen-printed carbon electrode and its direct electrochemistry and electrocatalysis, *Biosens. Bioelectron.* 74 (2015) 518–525.
- [21] L. Qi, C. Song, T. Wang, Q. Li, G.J. Hirasaki, R. Verduzco, Polymer-coated nanoparticles for reversible emulsification and recovery of heavy oil, *Langmuir* 34 (22) (2018) 6522–6528.
- [22] T. Hurrell, K.S. Lilley, A.D. Cromarty, Proteomic responses of HepG2 cell monolayers and 3D spheroids to selected hepatotoxins, *Toxicol. Lett.* 300 (2019) 40–50.
- [23] S. Mondal, P. Manivasagan, S. Bharathiraja, M. Santha Moorthy, V.T. Nguyen, H.H. Kim, S.Y. Nam, K.D. Lee, J. Oh, Hydroxyapatite coated iron oxide nanoparticles: a promising nanomaterial for magnetic hyperthermia cancer treatment, *Nanomaterials* 7 (12) (2017) 426.
- [24] A. Dabbagh, Z. Hedayatnasab, H. Karimian, M. Sarraf, C.H. Yeong, H.R. Madaah Hosseini, N.H. Abu Kasim, T.W. Wong, N. Abdul Rahman, Polyethylene glycol-coated porous magnetic nanoparticles for targeted delivery of chemotherapeutics under magnetic hyperthermia condition, *Int. J. Hyperthermia* 36 (1) (2019) 104–114.
- [25] P. Gas, E. Kurgan, Cooling effects inside water-cooled inductors for magnetic fluid hyperthermia, *Prog. Appl. Electr. Eng. (PAEE)* 2017 (2017) 1–4, <https://doi.org/10.1109/PAEE.2017.8008997>.
- [26] P.B. Shete, R.M. Patil, N.D. Thorat, A. Prasad, R.S. Ningthoujam, S.J. Ghosh, S.H. Pawar, Magnetic chitosan nanocomposite for hyperthermia therapy application: Preparation, characterization and in vitro experiments, *Appl. Surf. Sci.* 288 (2014) 149–157.
- [27] L.-Y. Zhang, H.-C. Gu, X.-M. Wang, Magnetite ferrofluid with high specific absorption rate for application in hyperthermia, *J. Magn. Magn. Mater.* 311 (1) (2007) 228–233.
- [28] A. Hervault, A.E. Dunn, M. Lim, C. Boyer, D. Mott, S. Maenosono, N.T. Thanh, Doxorubicin loaded dual pH- and thermo-responsive magnetic nanocarrier for combined magnetic hyperthermia and targeted controlled drug delivery applications, *Nanoscale* 8 (24) (2016) 12152–12161.
- [29] C.A. Quinto, P. Mohindra, S. Tong, G. Bao, Multifunctional superparamagnetic iron oxide nanoparticles for combined chemotherapy and hyperthermia cancer treatment, *Nanoscale* 7 (29) (2015) 12728–12736.
- [30] E. Ranjbari, M.R. Hadjmohammadi, F. Kiekens, K. De Wael, Mixed hemi/Ad-micelle sodium dodecyl sulfate-coated magnetic iron oxide nanoparticles for the efficient removal and trace determination of rhodamine-B and rhodamine-6G, *Anal. Chem.* 87 (15) (2015) 7894–7901.
- [31] M. Ravi, S. Song, J. Wang, R. Nadimicherla, Z. Zhang, Preparation and characterization of biodegradable poly(ε-caprolactone)-based gel polymer electrolyte films, *Ionics* 22 (5) (2016) 661–670.
- [32] W. Cai, J. Wan, Facile synthesis of superparamagnetic magnetite nanoparticles in liquid polyols, *J. Colloid Interface Sci.* 305 (2) (2007) 366–370.
- [33] S. Khoei, Y. Bagheri, A. Hashemi, Composition controlled synthesis of PCL-PEG Janus nanoparticles: magnetite nanoparticles prepared from one-pot photo-click reaction, *Nanoscale* 7 (9) (2015) 4134–4148.
- [34] D. Wilson, M. Langell, XPS analysis of oleylamine/oleic acid capped Fe₃O₄ nanoparticles as a function of temperature, *Appl. Surf. Sci.* 303 (2014) 6–13.
- [35] A. Manakhov, E.S. Permyakova, S. Ershov, A. Shevchyk, O. Kovalski, J. Polčák, I.Y. Zhitnyak, N.A. Glushankova, L. Zajíčková, D.V. Shtansky, Bioactive TiCaPCON-coated PCL nanofibers as a promising material for bone tissue

- engineering, *Appl. Surf. Sci.* 479 (2019) 796–802.
- [37] V.M. Correlo, L.F. Boesel, M. Bhattacharya, J.F. Mano, N.M. Neves, R.L. Reis, Properties of melt processed chitosan and aliphatic polyester blends, *Mater. Sci. Eng., A* 403 (1–2) (2005) 57–68.
- [38] Y. Zhong, V. Leung, L.Y. Wan, S. Dutz, F.K. Ko, U.O. Häfeli, Electrospun magnetic nanofibre mats—A new bondable biomaterial using remotely activated magnetic heating, *J. Magn. Magn. Mater.* 380 (2015) 330–334.
- [39] A. Weidner, C. Gräfe, M. Von der Lühse, H. Remmer, J.H. Clement, D. Eberbeck, F. Ludwig, R. Müller, F.H. Schacher, S. Dutz, Preparation of core-shell hybrid materials by producing a protein corona around magnetic nanoparticles, *Nanoscale Res. Lett.* 10 (1) (2015) 282–292.
- [40] G. Kandasamy, A. Sudame, T. Luthra, K. Saini, D. Maity, Functionalized hydrophilic superparamagnetic iron oxide nanoparticles for magnetic fluid hyperthermia application in liver cancer treatment, *ACS Omega* 3 (4) (2018) 3991–4005.
- [41] M. Von der Lühse, A. Weidner, S. Dutz, F.H. Schacher, Reversible electrostatic adsorption of polyelectrolytes and bovine serum albumin onto polyzwitterion-coated magnetic multicore nanoparticles: implications for sensing and drug delivery, *ACS Appl. Nano Mater.* 1 (1) (2017) 232–244.
- [42] P.S. Alemi, S.A. Atyabi, F. Sharifi, M. Mohamadali, S. Irani, H. Bakhshi, S.M. Atyabi, Synergistic effect of pressure cold atmospheric plasma and carboxymethyl chitosan to mesenchymal stem cell differentiation on PCL/CMC nanofibers for cartilage tissue engineering, *Polym. Adv. Technol.* 30 (6) (2019) 1356–1364.
- [43] E.A. Périgo, G. Hemery, O. Sandre, D. Ortega, E. Garaio, F. Plazaola, F.J. Teran, Fundamentals and advances in magnetic hyperthermia, *Appl. Phys. Rev.* 2 (4) (2015) 041302.
- [44] S. Dutz, R. Hergt, Magnetic nanoparticle heating and heat transfer on a microscale: Basic principles, realities and physical limitations of hyperthermia for tumour therapy, *Int. J. Hyperthermia* 29 (8) (2013) 790–800.
- [45] S. Laurent, S. Dutz, U.O. Häfeli, M. Mahmoudi, Magnetic fluid hyperthermia: Focus on superparamagnetic iron oxide nanoparticles, *Adv. Colloid Interface Sci.* 166 (1–2) (2011) 8–23.
- [46] Z. Hedayatnasab, F. Abnisa, W.M.A. Wan Daud, Investigation properties of superparamagnetic nanoparticles and magnetic field-dependent hyperthermia therapy, *IOP Conf. Ser.: Mater. Sci. Eng.* 334 (1) (2018) 012042.
- [47] P. Gas, A. Miaskowski, Specifying the ferrofluid parameters important from the viewpoint of magnetic fluid hyperthermia, *Selected Problems of Electrical Engineering and Electronics (WZEE) 2015* (2015) 1–6, <https://doi.org/10.1109/WZEE.2015.7394040>.
- [48] M. Kubovcikova, M. Koneracka, O. Strbak, M. Molcan, V. Zavisova, I. Antal, I. Khmara, D. Lucanska, L. Tomco, M. Barathova, M. Zatovicova, D. Dobrota, S. Pastorekova, P. Kopcansky, Poly-L-lysine designed magnetic nanoparticles for combined hyperthermia, magnetic resonance imaging and cancer cell detection, *J. Magn. Magn. Mater.* 475 (2019) 316–326.
- [49] G. Shi, R. Takeda, S.B. Trisnanto, T. Yamada, S. Ota, Y. Takemura, Enhanced specific loss power from Resovist® achieved by aligning magnetic easy axes of nanoparticles for hyperthermia, *J. Magn. Magn. Mater.* 473 (2019) 148–154.
- [50] E. Kurgan, P. Gas, Simulation of the electromagnetic field and temperature distribution in human tissue in RF hyperthermia, *Prz. Elektrotech.* 91 (2015) 169–172, <https://doi.org/10.15199/48.2015.01.37>.
- [51] L. Kafrouni, O. Savadogo, Recent progress on magnetic nanoparticles for magnetic hyperthermia, *Prog. Biomater.* 5 (3–4) (2016) 147–160.
- [52] A.E. Deatsch, B.A. Evans, Heating efficiency in magnetic nanoparticle hyperthermia, *J. Magn. Magn. Mater.* 354 (2014) 163–172.